Materials Research Bulletin 47 (2012) 4137–4145

Contents lists available at SciVerse ScienceDirect

Materials Research Bulletin

journal homepage: www.elsevier.com/locate/matresbu

Large-scale synthesis of $Lu_2O_3:Ln^{3+}$ ($Ln^{3+} = Eu^{3+}, Tb^{3+}, Yb^{3+}/Er^{3+}, Yb^{3+}/Tm^{3+}$, and Yb^{3+}/Ho^{3+}) microspheres and their photoluminescence properties

Yu Gao [a,*], Jian Gong [b], Miaomiao Fan [c], Qinghong Fang [a,*], Na Wang [a], Wenchi Han [a], Zhenhe Xu [a,*]

[a] College of Materials Science and Engineering, Shenyang University of Chemical Technology, Shenyang 110142, PR China
[b] Key Laboratory of Polyoxometalate Science of Ministry of Education, Department of Chemistry, Northeast Normal University, Changchun, Jilin 130024, PR China
[c] Department of Medical Pharmaceutical, Shenyang Chemical Industry School, Shenyang 110142, PR China

ARTICLE INFO

Article history:
Received 17 June 2012
Received in revised form 7 August 2012
Accepted 28 August 2012
Available online 4 September 2012

Keywords:
A. Inorganic compounds
A. Nanostructures
A. Optical materials
C. X-ray diffraction
D. Luminescence

ABSTRACT

In this work, multicolor and monodisperse $Lu_2O_3:Ln^{3+}$ ($Ln^{3+} = Eu^{3+}, Tb^{3+}, Yb^{3+}/Er^{3+}, Yb^{3+}/Tm^{3+}$, and Yb^{3+}/Ho^{3+}) microspheres were prepared by a homogeneous precipitation method followed by a subsequent calcination process. X-ray diffraction (XRD), Fourier transformed infrared (FT-IR), thermogravimetric analysis (TGA), scanning electron microscopy (SEM), transmission electron microscopy (TEM), photoluminescence (PL) spectra, and cathodoluminescence (CL) spectra were employed to characterize the samples. Upon ultraviolet and low-voltage electron beams excitation, $Lu_2O_3:Ln^{3+}$ ($Ln^{3+} = Eu^{3+}$ and Tb^{3+}) samples exhibit respective bright red (Eu^{3+}, $^5D_0 \rightarrow {}^7F_2$) and green ($Tb^{3+}$, $^5D_4 \rightarrow {}^7F_5$) down-conversion (DC) emissions. Under 980 nm NIR irradiation, $Lu_2O_3:Ln^{3+}$ ($Ln^{3+} = Yb^{3+}/Er^{3+}, Yb^{3+}/Tm^{3+}$, and Yb^{3+}/Ho^{3+}) exhibit characteristic up-conversion (UC) emissions of green (Er^{3+}, $^4S_{3/2}, {}^2H_{11/2} \rightarrow {}^4I_{15/2}$), blue ($Tm^{3+}$, $^1G_4 \rightarrow {}^3H_6$) and yellow-green ($Ho^{3+}$, $^5F_4, {}^5S_2 \rightarrow {}^5I_8$), respectively. These finding may find potential applications in bioanalysis, optoelectronic and nanoscale devices, field emission displays, and so on.

1. Introduction

The development of nano- or micromaterials with size- and shape-controlled morphologies may open new opportunities in exploring the chemical and physical properties of the materials [1]. Thus far, dramatic efforts have been dedicated to develop new methods for the fabrication of a range of high-quality inorganic nanostructures in different systems. From the perspective of applications, nanomaterials are not only synthesized in large quantities with a desired composition, reproducible size, shape, and structure but also prepared and assembled using simplicity, low costs, ease of scale-up, and relative greenness (aqueous solution) constitute the key trains of this method [2,3]. Therefore, the development of a mild and more controlled method for creating such novel architectures will be of general interest.

Recently, much research attention has been paid to the field of rare earth materials since they have many potential applications based on their novel electronic and optical properties resulting from their 4f electrons [4–10]. Among the various rare earth materials, rare earth oxide phosphor is a kind of advanced materials which offer unique spectral properties, such as large Stokes shifts, narrow emission bandwidths, long fluorescence lifetimes and suitability for multiphoton excitation [11–14]. Based on the attractive optical characteristics arising from the 4f–5d electron transition [15–25], the rare earth oxide phosphors have been recognized to hold tremendous applications in the fields of high performance luminescent devices, optoelectronic devices, sensors, catalysts, MRI contrast agents, fluorescent labels and other functional materials [26–28,12,29–31]. As we know, lutetium oxide (Lu_2O_3) is an excellent candidate due to its favorable physical properties, such as high melting point, phase stability, and low thermal expansion [32]. Ln^{3+}-doped Lu_2O_3 materials (Ln^{3+} = Eu, Tb, Er, Ho, Sm) are important phosphors as reported in previous studies [33–39]. So far, various traditional synthesis methods have been used to prepare Lu_2O_3 and Ln^{3+}-doped Lu_2O_3 materials, such as a combustion process using urea, glycine, and citric acid as fuel [33–36], a coprecipitation method [37,38], the Pechini sol–gel procedure [39], and hydrothermal methods [40,41]. These synthesis techniques are well-known and routinely used for fabrication of oxide phosphors. In addition, inorganic particles always show unique size- and shape-dependent properties, such as shape, size, crystallinity, defects, grain boundaries, crystal structure, and preparation technique. Also, the uniform spherical nanoparticles which present lower surface defects are preferred for improving optical properties [42]. However, research on Lu_2O_3 phosphors has mainly been focused on Eu^{3+} doped one-dimensional nanostructures, such as nanorods and nanofibers [40]. There

* Corresponding author. Tel.: +86 24 89388153; fax: +86 24 89388153.
E-mail address: gaoy777@126.com (Y. Gao).

0025-5408/$ – see front matter © 2012 Elsevier Ltd. All rights reserved.
http://dx.doi.org/10.1016/j.materresbull.2012.08.065

have been few reports related to the fabrication of zero-dimensional Lu_2O_3 nanoparticles, especially employing rare earth ions as dopants to study their luminescent properties. Furthermore, the products usually possess poor monodispersity and uniformity, and the methods (such as hydrothermal synthesis) are not suitable for large-scale and industrial preparation.

In the present work, we report a controllable route for the production of well-dispersed, multicolored and spherical $Lu_2O_3:Ln^{3+}$ phosphors. First, we present a simple and mass production urea homogeneous precipitation method to fabricate $Lu(OH)CO_3:Ln^{3+}$ precursor spheres at low temperatures without any templates. Then, the $Lu_2O_3:Ln^{3+}$ microspheres can be obtained after the calcination process. This approach is of significant importance in industrial applications as a consequence of its low costs, mass production, and synthetic convenience. And the possible formation mechanism of the microspheres is proposed. As an example of potential application, various lanthanide ions ($Ln^{3+} = Eu^{3+}$, Tb^{3+}, Yb^{3+}/Er^{3+}, Yb^{3+}/Tm^{3+}, and Yb^{3+}/Ho^{3+}) have been doped into the microspheres, and the corresponding luminescent properties have been also investigated in detail.

2. Experimental

2.1. Materials

The initial chemicals, including Lu_2O_3, Eu_2O_3, Tb_4O_7, Er_2O_3, Tm_2O_3 Yb_2O_3, and Ho_2O_3 (all with purity ≥ 99.99%) were purchased from Science and Technology Parent Company of Changchun Institute of Applied Chemistry, and other chemicals were purchased from Beijing Chemical Company, China. All chemicals are of analytical grade reagents and used directly without further purification.

2.2. Preparation of monodisperse Lu_2O_3 and $Lu_2O_3:Ln^{3+}$ spheres

The monodisperse colloid spheres of $Lu(OH)CO_3$ were prepared *via* a urea-based homogeneous precipitation process [43,44]. A total of 0.75 mL of $Lu(NO_3)_3$ (1 M) and 1.5 g of urea $[CO(NH_2)_2]$ were dissolved in deionized water. The total volume of the solution was about 50 mL. The above solution was first homogenized under magnetic stirring at room temperature for 2 h. The resultant solution was then reacted at 90 °C for 2 h in the oil bath. The obtained suspension was separated by centrifugation and collected after washing with deionized water several times. The rare-earth doped $Lu(OH)CO_3:Ln^{3+}$ colloid spheres were prepared by the same procedures for the $Lu(OH)CO_3$ sample except that a stoichiometric amount of $Ln(NO_3)_3$ aqueous solutions was added to $Lu(NO_3)_3$ for the precursors in the initial stage as described above. The doping concentration of the Eu^{3+}, Tb^{3+}, Yb^{3+}/Er^{3+}, Yb^{3+}/Tm^{3+}, and Yb^{3+}/Ho^{3+}) was 5 mol%, 5 mol%, 3 mol%/1 mol%, 3 mol%/1 mol%, and 3 mol%/1 mol%, to Lu^{3+} in $Lu(OH)CO_3:Ln^{3+}$, respectively. Subsequently, the precursor was calcined from room temperature to 800 °C with a heating rate of 1 °C min^{-1} and maintained at this temperature for 4 h. In this way, the Lu_2O_3 microspheres were obtained. Other $Lu_2O_3:Ln^{3+}$ samples were prepared by a similar procedure except for using different doping lanthanide ions.

2.3. Characterization

The X-ray diffraction (XRD) patterns of the samples were recorded on a D8 Focus diffractometer (Bruker) with CuKa radiation (λ = 0.15405 nm). Fourier transform infrared spectroscopy (FT–IR) spectra were measured with a Perking-Elmer 580B infrared spectrophotometer with the KBr pellet technique. Thermogravimetric data were recorded with Thermal Analysis instrument (SDT 2960, TA Instruments, New Castle, DE) with the heating rate of 10 °C min^{-1} in an air flow of 100 mL min^{-1}. The morphologies and composition of the as-prepared samples were inspected on a field emission scanning electron microscope (FE-SEM, S4800, Hitachi). Low- and high-resolution transmission electron microscopy (TEM) was performed by using an FEI Tecnai G2 S-Twin instrument with a field emission gun operating at 200 kV. Images were acquired digitally on a Gatan multiople CCD camera. The ultraviolet–visible photoluminescence (PL) excitation and emission spectra were recorded with a Hitachi F-7000 spectrophotometer equipped with a 150 W xenon lamp as the excitation source. The cathodoluminescent (CL) measurements were carried out in an ultrahigh-vacuum chamber (10^{-8} torr), where the phosphors were excited by an electron beam at a voltage range of 1–5 kV, and the spectra were recorded using an F-7000 spectrophotometer. The UC emission spectra were obtained using a 980 nm laser from an OPO (optical parametric oscillator, Continuum Surelite, USA) as the excitation source and detected by R955 (HAMAMATSU) from 400 to 900 nm. All measurements were performed at room temperature.

3. Results and discussion

3.1. Phase structure, morphology, and formation process

The structure characterizations are typically performed on the Lu_2O_3:5 mol% Eu^{3+} sample. The other samples are similar to those of Lu_2O_3:5 mol% Eu^{3+} sample and will not be shown here. The composition and phase purity of the samples were first investigated by XRD. Fig. 1 shows the XRD patterns of the as-prepared precursor for $Lu(OH)CO_3$:5 mol% Eu^{3+} sample, and those annealed from 400–800 °C as well as the JCPDS card No. 86-2475) for Lu_2O_3, respectively. The XRD pattern of the precursor shows two broad bands at $2\theta = 30°$ and 45° (Fig. 1A), which indicates that the sample is amorphous. Annealing the material for 4 h at temperature as high as 400 °C resulted in no significant change in powder XRD, and the material displayed a amorphous pattern that is consistent with $Lu(OH)CO_3$:5 mol% Eu^{3+} sample with no other detectable phases (Fig. 1B). With increasing the annealing temperature to 600 °C (Fig. 1C), and then to 700 °C (Fig. 1D), all the diffraction peaks increase in intensity due to the increase of crystallinity. For the sample annealed at 800 °C (Fig. 1E), well defined diffraction peaks appear, and can coincide well with the cubic phase of Lu_2O_3 [space group: Ia $\bar{3}$(2 0 6)], which is consistent with the values in the standard cards [JCPDS No. 86-2475]. No additional peaks for other phases have been found, indicating that the precursor sample has fully crystallized into Lu_2O_3 at this heating temperature. No obvious shifting of peaks or other impurity phase can be detected

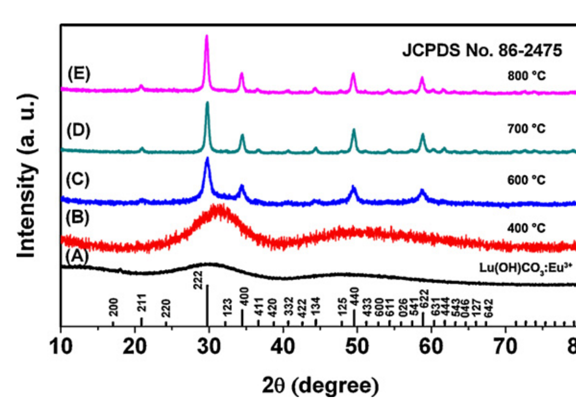

Fig. 1. (A) XRD patterns of the as-obtained $Lu(OH)CO_3:Eu^{3+}$ precursor, and precursor annealed at (B) 400 °C, (C) 600 °C, (D) 700 °C, and (E) 800 °C as well as JCPDS card 86-2475 of Lu_2O_3 for comparison.

at the current doping level, indicating that the Eu^{3+} ions are efficiently dissolved in the Lu_2O_3 host lattice by replacing the Lu^{3+}.

The morphologies and microstructure details of the $Lu(OH)CO_3:Eu^{3+}$ precursor are characterized by SEM and TEM techniques, as given in Fig. 2. Images A and B in Fig. 2 show the low- and high-magnification SEM images of the as-prepared $Lu(OH)CO_3:Eu^{3+}$ precursor. From Fig. 2A it can be clearly seen that the $Lu(OH)CO_3:Eu^{3+}$ sample is composed of a large scale of uniform and monodisperse spherical particles with an average diameter of 100 nm, and these particles present a smooth surface and narrow size distribution, suggesting the high yield achieved with this approach. More careful examination of the high-magnification SEM image (Fig. 2B) shows that the surface of the particles is smooth. To further study the fine structure of the above spheres, a representative TEM micrograph for $Lu(OH)CO_3:Eu^{3+}$ spheres is shown in Fig. 2C, clearly showing that the products are entirely composed of spherical particles with an average diameter of 100 nm, consistent with the values shown in the SEM image (Fig. 2B). The chemical composition of the $Lu(OH)CO_3:Eu^{3+}$ particles was further investigated with energy-dispersive X-ray (EDX) spectroscopy, which indicates that the spheres were made of lutetium (Lu), europium (Eu), oxygen (O), and carbon (C) elements (Fig. 2D).

Well-dispersed $Lu(OH)CO_3$ particles were used as precursor to fabricate Lu_2O_3 crystals. On the basis of TGA data (Fig. 3A), the $Lu(OH)CO_3$ sample was calcined from room temperature to 800 °C with a total weight loss of 26.57% and maintained at this temperature for 4 h for ensuring their complete decomposition, and phase-pure Lu_2O_3 was obtained. In Fig. 3B for the as-formed precursor sample, the FT-IR spectrum shows the characteristic absorption bands at 1531, 1399, 1084, 840 cm^{-1} which are assigned to the respective CO (ν_{as}), CO (ν_{as}), CO (ν_s) and CO (δ) (ν_s = symmetric stretch; ν_{as} = asymmetric stretch; and δ = deformation) in the CO_3^{2-} groups, revealing the composition of the precursor (red line) [45]. After annealing the as-formed precursor sample at 800 °C (Fig. 3B), a strong absorption band at 581 cm^{-1} for the stretching vibration of Lu–O [46,47] appears. Furthermore, almost all the functional groups related with $Lu(OH)CO_3:Eu^{3+}$ precursor disappear, suggesting the complete transformation from the $Lu(OH)CO_3:Eu^{3+}$ precursor to the final $Lu_2O_3:Eu^{3+}$ product.

For the calcined Lu_2O_3:5 mol% Eu^{3+} sample, the morphology of the obtained Lu_2O_3:5 mol% Eu^{3+} has been investigated and shown in Fig. 4. The low-magnification (Fig. 4A) and high-magnification (Fig. 4B) SEM images of Lu_2O_3:5 mol% Eu^{3+} samples clearly indicate that calcination at temperature of 800 °C does not cause any significant changes in the spherical morphology, and the products consist of large-scale, monodisperse spheres. The Lu_2O_3 spheres inherit their parents' morphology, but their size is shrunk in comparison with $Lu(OH)CO_3$ spheres in that the density of the former is higher than that of the latter. Closer observation reveals that there are cracks on the surface of the spheres, which may be attributed to the removal of H_2O and CO_2 from the constituent OH^- and CO_3^{2-} groups in the precursor during the calcination process. The result indicates that Lu_2O_3:5 mol% Eu^{3+} sphere have been successfully obtained, and the morphologies are well-inherited from $Lu(OH)CO_3$ spheres except for the cracks on the surface. Nevertheless, the conversion does not lead to the change in the morphology and such a transformation is common for rare earth hydroxide compounds decomposition [48–51,8]. The morphologies can be maintained perhaps because of the higher activation energies needed for the collapse of these structures [52,53]. Thus, high-quality Lu_2O_3:5 mol% Eu^{3+} spheres can be fabricated in a large scale using this method. To further study the fine structure of the above Lu_2O_3:5 mol% Eu^{3+} spheres, TEM was performed. Fig. 4C shows a typical TEM image of the Lu_2O_3:5 mol% Eu^{3+} spheres. It can be observed that the calcined sample is also spheres. In the high-resolution transmission electron microscopy (HRTEM) image (Fig. 4D), the lattice fringes are obvious and the distance of 0.300 nm between the adjacent lattice fringes match with the respective d_{222} value (0.299 nm) of cubic Lu_2O_3 structure (JCPDS

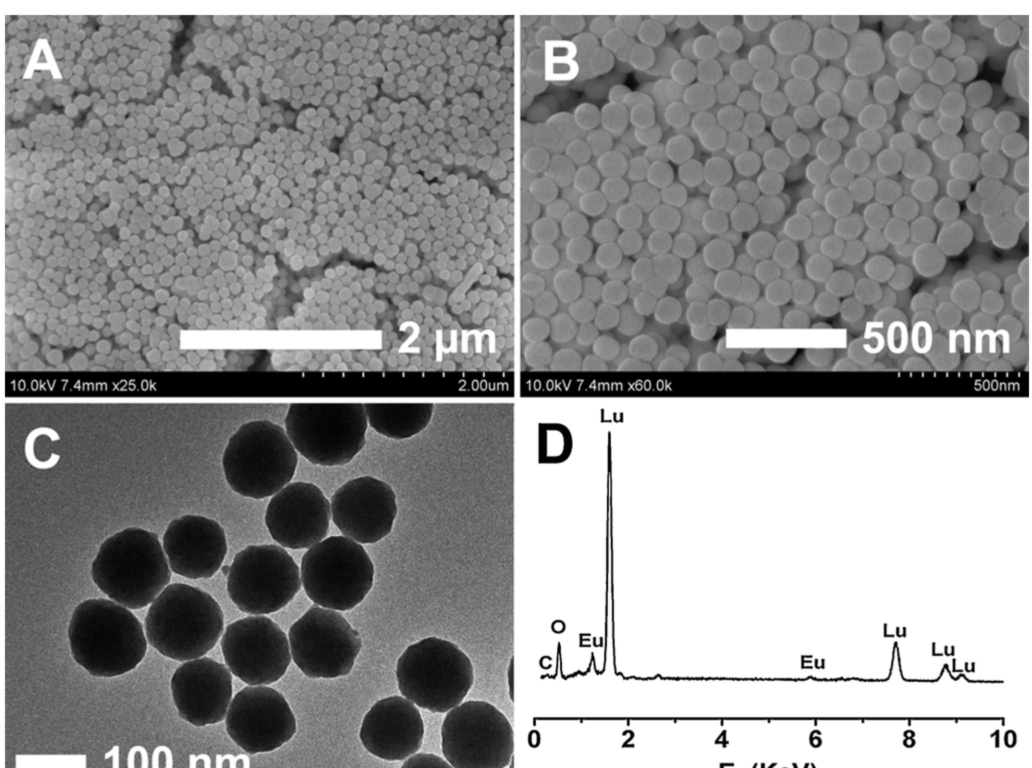

Fig. 2. (A) Low-magnification SEM image, (B) high-magnification SEM image, (C) TEM image, and (D) EDX of $Lu(OH)CO_3:Eu^{3+}$ precursor.

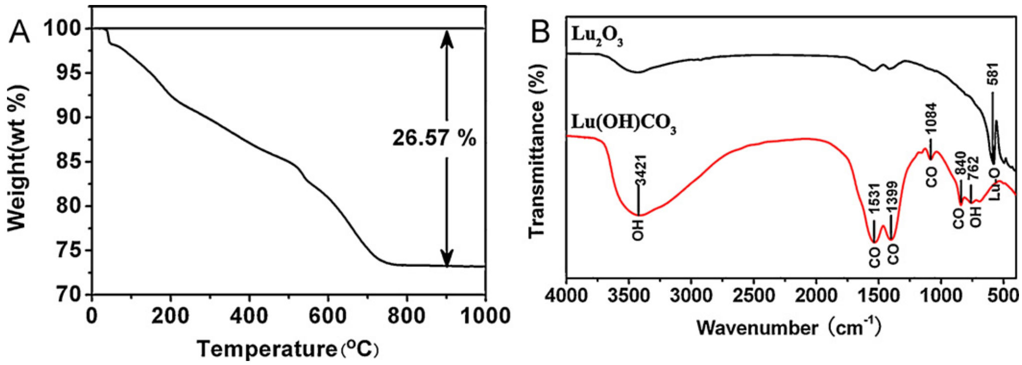

Fig. 3. (A) TGA curve of $Lu(OH)CO_3:Eu^{3+}$ precursor, and (B) FT-IR spectra of $Lu(OH)CO_3:Eu^{3+}$ precursor and $Lu_2O_3:Eu^{3+}$ microspheres. (For interpretation of the references to color in this figure legend, the reader is referred to the web version of this article.)

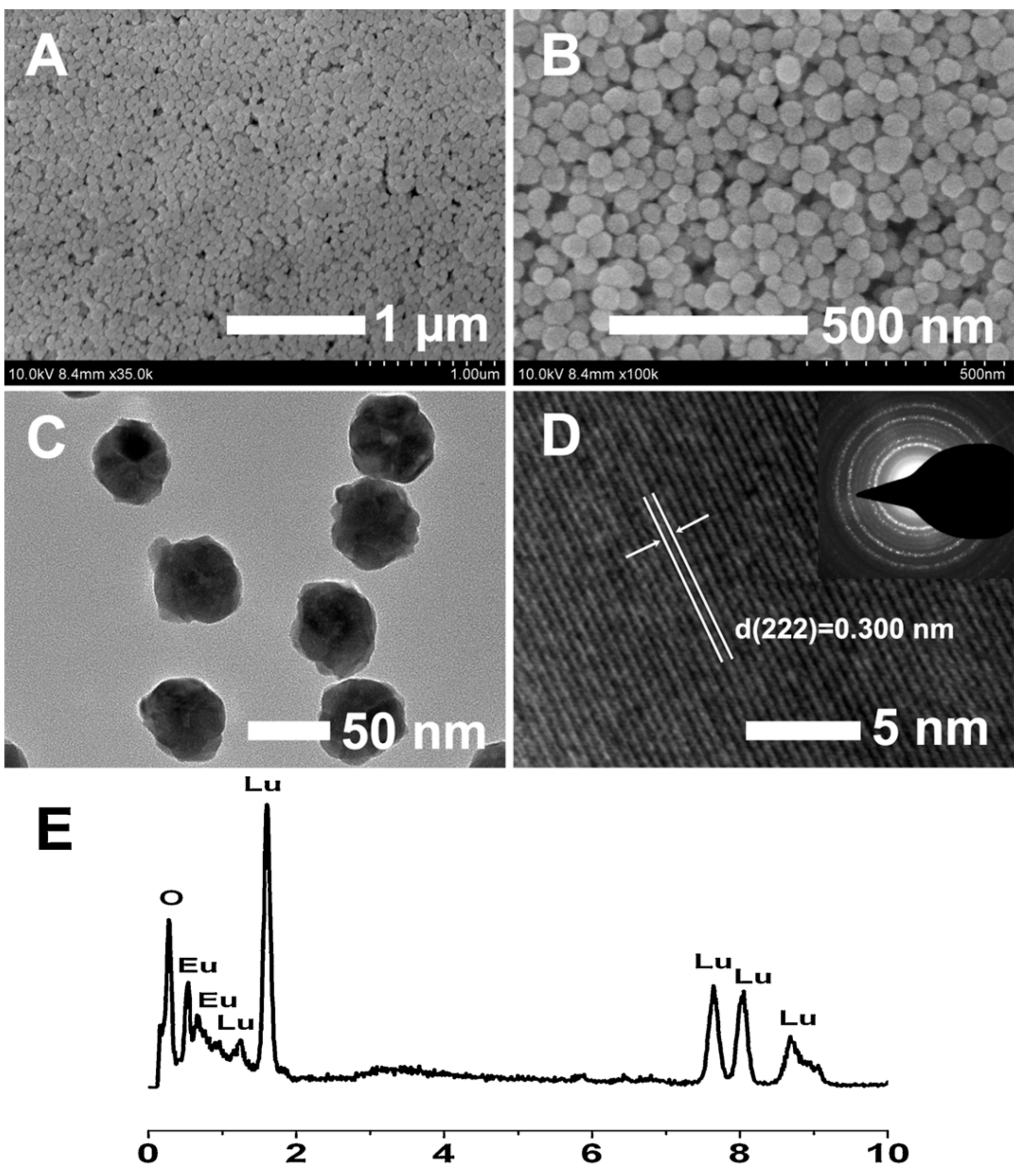

Fig. 4. (A) Low-magnification SEM image, (B) high-magnification SEM image, (C) TEM image, (D) HRTEM image, and (E) EDX of $Lu_2O_3:Eu^{3+}$ microspheres.

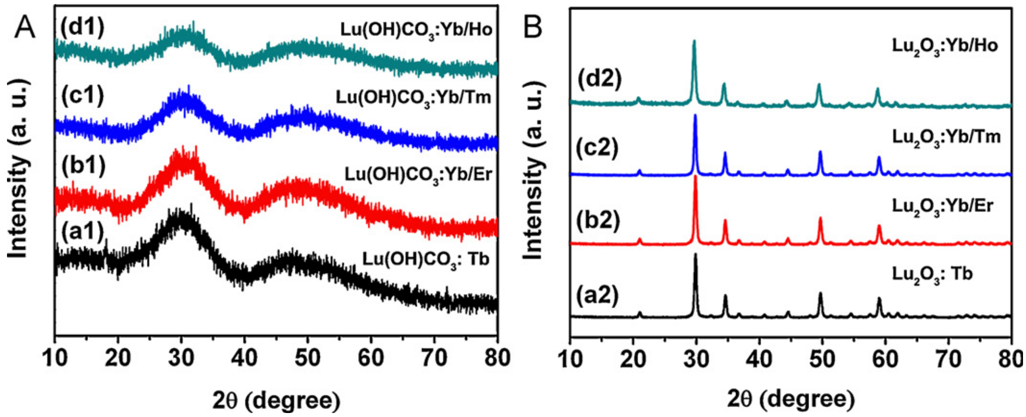

Fig. 5. (A) XRD patterns of as-prepared other $Lu(OH)CO_3:Ln^{3+}$ precursors, and (B) the $Lu_2O_3:Ln^{3+}$ products.

No. 86-2475). The EDX was used to further characterize the chemical composition of the as-prepared Lu_2O_3:5 mol% Eu^{3+} samples. The EDX spectrum (Fig. 4E) shows the presence of Lu, Eu, and O elements. From the EDX spectrum, the atom ratio of the calcined sample (O/Lu = 1.51/1) can be calculated, which is in accordance with the stoichiometric atomic ratio of the Lu_2O_3 products, and the EDX result gives further support for the XRD analysis above.

In addition, it should be mentioned that the existence of other lanthanide ions in Lu_2O_3 did not change the phase, crystallization, and morphology of the products in our present work. Other $Lu_2O_3:Ln^{3+}$ ($Ln^{3+} = Tb^{3+}$, Yb^{3+}/Er^{3+}, Yb^{3+}/Tm^{3+}, and Yb^{3+}/Ho^{3+}) samples were prepared by a similar procedure except for using different doping lanthanide ions. The precursors $Lu(OH)CO_3:Ln^{3+}$ ($Ln^{3+} = Tb^{3+}$, Yb^{3+}/Er^{3+}, Yb^{3+}/Tm^{3+}, and Yb^{3+}/Ho^{3+}) show two broad bands at $2\theta = 30^\circ$ and 45° (Fig. 5A), which indicates that the samples are amorphous. After subsequent heat treatment at 800 °C in air for 4 h, the Ln^{3+}-doped lutetium oxide precursor transforms into cubic Lu_2O_3, as identified in Fig. 5B. The TEM images of other $Lu_2O_3:Ln^{3+}$ samples are displayed in Fig. 6. It can be seen that all

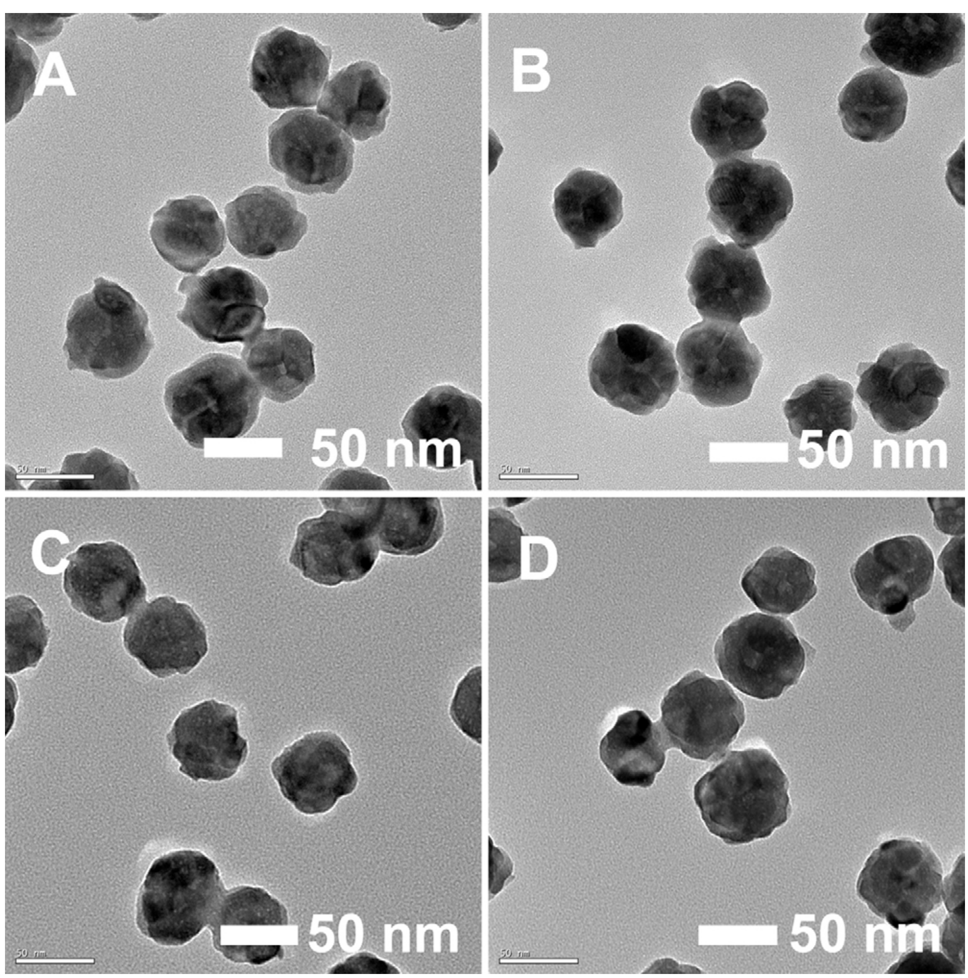

Fig. 6. TEM images of (A) $Lu_2O_3:Tb^{3+}$, (B) $Lu_2O_3:Yb^{3+}/Er^{3+}$, (C) $Lu_2O_3:Yb^{3+}/Tm^{3+}$, and (D) $Lu_2O_3:Yb^{3+}/Ho^{3+}$ samples.

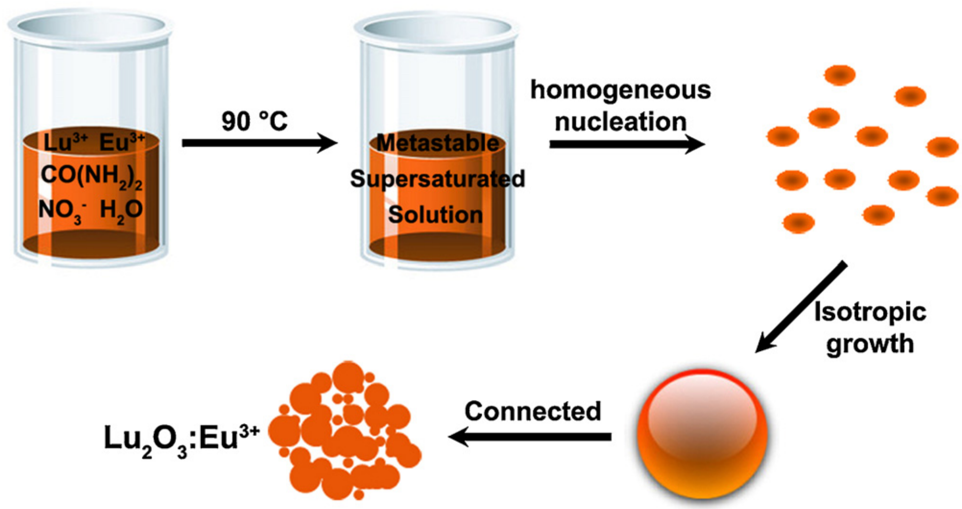

Scheme 1. Schematic illustration for the formation process of $Lu_2O_3:Eu^{3+}$ microspheres.

the samples have similar particle size and morphology, suggesting that small amounts of doping components have little influence on the final products.

3.2. Formation mechanism for the $Lu_2O_3:Eu^{3+}$ spheres

The possible schematic illustration of formation mechanism of this spherical structure is shown in Scheme 1. There are three main chemical reactions existing during the above mentioned phase and morphological evolution:

$$CO(NH_2)_2 + H_2O \leftrightarrow 5CO_2 + 2NH_3 \quad (1)$$

$$NH_3 + H_2O \leftrightarrow NH_4{}^+ + OH^- \quad (2)$$

$$0.95Lu^{3+} + 0.05Eu^{3+} + 3OH^- + CO_2 \rightarrow Lu_{0.95}Eu_{0.05}(OH)CO_3 + H_2O \quad (3)$$

At the initial stage of the reaction, due to Eq. (1), the hydrolysis of urea can produce CO_2 and NH_3. Then, the hydrolysis of NH_3 can produce OH^- ions due to reaction (2). As the reaction proceeds, the supersaturation reaches the nucleation concentration, large numbers of the $Lu_{0.95}Eu_{0.05}(OH)CO_3$ (namely $Lu(OH)CO_3:Eu^{3+}$) seeds form simultaneously and rapidly through a homogeneous nucleation process (Eq. (3)). Simultaneously, the supersaturation concentration is lower than the nucleation concentration, and $Lu(OH)CO_3:Eu^{3+}$ seeds re-crystallize and grow into uniform spherical nanoparticles *via* a highly isotropic growth process. Until the concentration of the solution below the saturation, the growth process is finished and $Lu(OH)CO_3:Eu^{3+}$ precursor is formed by the above homogeneous precipitation process.

Subsequently, the as-prepared $Lu(OH)CO_3:Eu^{3+}$ precursor was calcined from room temperature to 800 °C with a heating rate of 1 °C min^{-1} and maintained at this temperature for 4 h. Before the calcination temperature reaches the decomposition point of $Lu(OH)CO_3:Eu^{3+}$ precursor, the dehydration of crystal water occurs according to TG-DTA result. As the temperature rises, the condensation reaction leads to the nucleation of $Lu(OH)CO_3:Eu^{3+}$ at a critical supersaturation. And the formed $(Lu_{0.95}Eu_{0.05})_2O_3$ (namely $Lu_2O_3:Eu^{3+}$) nuclei will grow slowly up into ultrafine crystallites under the heating rate of 1 °C min^{-1}. Then many ultrafine crystallites are combined into small nanocrystallites through mass transport, while the H_2O and CO_2 would be further evaporated. And the following reaction may take place:

$$2Lu_{0.95}Eu_{0.05}(OH)CO_3 \rightarrow 2(Lu_{0.95}Eu_{0.05})_2O_3 + H_2O + 2CO_2 \quad (4)$$

The formation of $Lu_2O_3:Eu^{3+}$ is also experienced nucleation and growth process. However, the most difference is the heterogeneous nucleation and growth of the calcination process.

3.3. Luminescent properties

Our experimental results and previous investigations have shown that cubic Lu_2O_3 is a good host lattice for the luminescence of various optically active lanthanide ions, just like the same type of Y_2O_3 [37,35,34]. The PL excitation and emission spectra of the $Lu_2O_3:Eu^{3+}$ sample is shown in Fig. 7A. The excitation spectra of the $Lu_2O_3:Eu^{3+}$ samples consist of a strong absorption band centered at

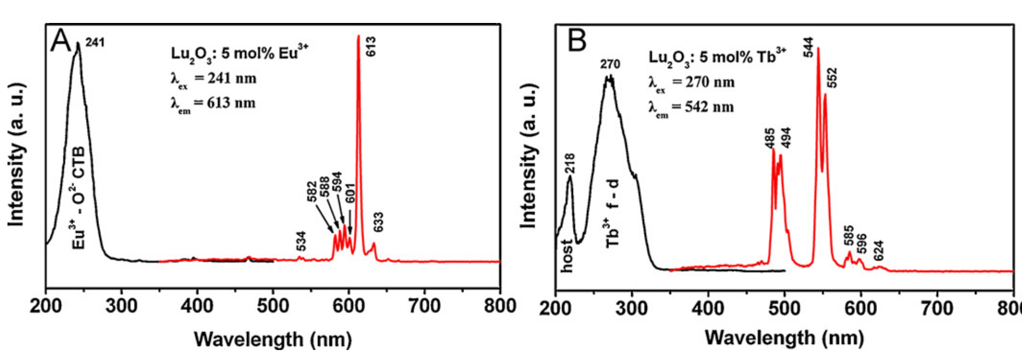

Fig. 7. PL excitation and emission spectra of (A) $Lu_2O_3:Eu^{3+}$, and (B) $Lu_2O_3:Tb^{3+}$ samples.

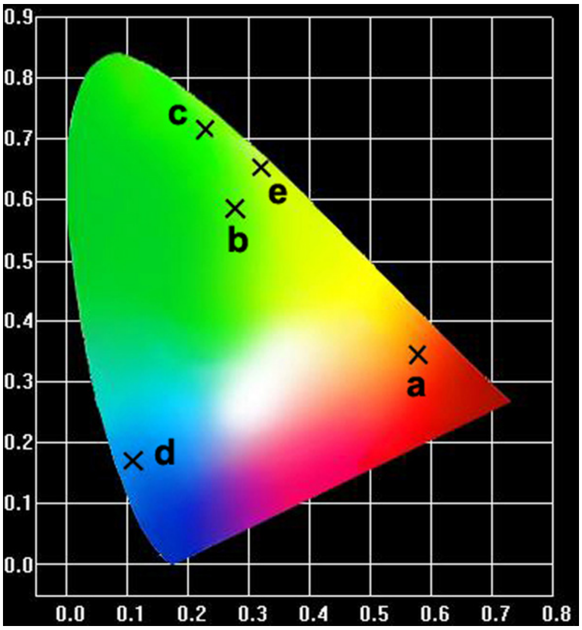

Fig. 8. CIE chromaticity diagram showing the emission colors for the as-prepared (A) Lu_2O_3:Eu^{3+}, (B) Lu_2O_3:Tb^{3+}, (C) Lu_2O_3:Yb^{3+}/Er^{3+}, (D) Lu_2O_3:Yb^{3+}/Tm^{3+}, and (E) Lu_2O_3:Yb^{3+}/Ho^{3+}.

241 nm and some weak lines, which are due to the charge transfer band (CTB) between the O^{2-} and Eu^{3+} ions and the f→f transitions of the Eu^{3+} ions, respectively (Fig. 7A, left). Upon excitation at 241 nm, the emission spectra of Lu_2O_3:Eu^{3+} sample is composed of a group of lines at about 534, 582, 588, 594, 601, 613, and 633 nm, which can be attributed to $^5D_0 \rightarrow {}^7F_J$ (J = 0, 1, 2, 3, 4) transition lines of the Eu^{3+} ions, respectively (Fig. 7A, right). The emission spectrum is dominated by the red $^5D_0 \rightarrow {}^7F_2$ (613 nm) transition of Eu^{3+}, which is an electric-dipole allowed transition and hypersensitive to the environment. The corresponding CIE (Commission Internationale de l'Eclairage 1931 chromaticity) coordinates for the emission spectrum of Lu_2O_3:Eu^{3+} are determined as x = 0.5785, y = 0.3460, located in the red region (point a, Fig. 8).

As for Lu_2O_3:Tb^{3+} sample, the excitation spectrum (Fig. 7B, left) mainly consists of two peaks at 218 and 270 nm, which can be attributed to the Lu_2O_3 host absorption and f→d energy transfer in Tb^{3+}, respectively. The obtained emission spectrum (Fig. 7B, right) of Lu_2O_3:Tb^{3+} consists of f→f transition lines within $(4f)^8$ electron configuration of Tb^{3+}, i.e. $^5D_4 \rightarrow {}^7F_6$ (485 nm) in the blue region and $^5D_4 \rightarrow {}^7F_5$ (544 nm) in the green region, as well as $^5D_4 \rightarrow {}^7F_4$ (585 nm) and $^5D_4 \rightarrow {}^7F_3$ (624 nm) in the red region. The strongest one is located at 544 nm corresponding to $^5D_4 \rightarrow {}^7F_5$ transition of Tb^{3+}. The corresponding CIE coordinated for the emission spectrum of Lu_2O_3:Tb^{3+} are determined as x = 0.2763, y = 0.5853, which is located in the green region (point b, Fig. 8). In summary, the results demonstrate that the Lu_2O_3 microspheres material is a promising host for doping rare earth ions and meets the requirement of exploring phosphors with excellent red and green color purity.

Fig. 9 shows the up-conversion (UC) luminescence spectra of Yb^{3+}/Ln^{3+} (Ln^{3+} = Er, Tm, Ho) doped Lu_2O_3 under 980 nm laser excitation, and their corresponding photographs under 980 nm irradiation. The Lu_2O_3:Yb^{3+}/Er^{3+}, Lu_2O_3:Yb^{3+}/Tm^{3+}, and Lu_2O_3:Yb^{3+}/Ho^{3+} samples exhibit bright green, whitish blue, and green emissions, respectively, which evidently can be confirmed by the luminescence photographs under 980 nm light excitation (insets in Fig. 9). Fig. 9A shows the UC emission spectrum of the Lu_2O_3:Yb^{3+}/Er^{3+} sample excited at 980 nm. The emission bands centered at 522, 541 and 662 nm can be assigned to $^2H_{11/2} \rightarrow {}^4I_{15/2}$ (green), $^4S_{3/2} \rightarrow {}^4I_{15/2}$ (green) and $^4F_{9/2} \rightarrow {}^4I_{15/2}$ (red) transitions of

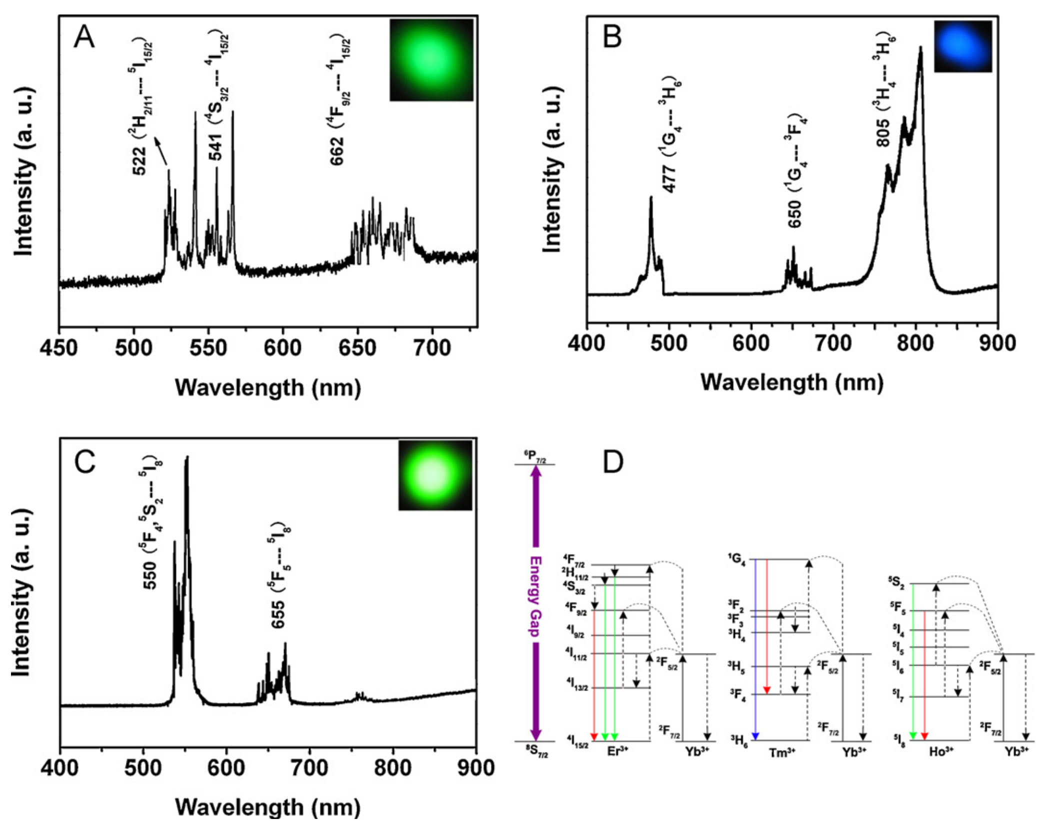

Fig. 9. NIR-to-visible UC emission spectra of (A) Lu_2O_3:Yb^{3+}/Er^{3+}, (B) Lu_2O_3:Yb^{3+}/Tm^{3+}, (C) Lu_2O_3:Yb^{3+}/Ho^{3+} under 980 nm laser excitation, and (D) the proposed energy transfer mechanisms under 980 nm diode laser excitation in Lu_2O_3:Yb^{3+}/Er^{3+}, Lu_2O_3:Yb^{3+}/Tm^{3+}, and Lu_2O_3:Yb^{3+}/Ho^{3+}.

Er^{3+}, respectively [54–56]. The corresponding CIE coordinates for the emission spectrum of Lu_2O_3:Yb^{3+}/Er^{3+} are determined as $x = 0.228$, $y = 0.714$, located in the green region (point c, Fig. 8). In the UC emission spectrum of Lu_2O_3:Yb^{3+}/Tm^{3+} (Fig. 9B), the three emission bands centered at 477, 650, and 805 nm can be attributed to the $^1G_4 \rightarrow {}^3H_6$ (blue), $^1G_4 \rightarrow {}^3F_4$ (red), and $^3H_4 \rightarrow {}^3H_6$ (red) transition of the Tm^{3+} ion. The corresponding CIE coordinates for the emission spectrum of Lu_2O_3:Yb^{3+}/Tm^{3+} are determined as $x = 0.1109$, $y = 0.1690$, located in the green region (point d, Fig. 8). The UC spectrum (Fig. 9C) of Lu_2O_3:Yb^{3+}/Ho^{3+} shows intense green emission centered at 550 nm and, which can be attributed to the $^5F_4$, $^5S_2 \rightarrow {}^5I_8$ (green) transition of the Ho^{3+} ion. The notably weaker emission at 655 nm is ascribed to the transition of $^5F_5 \rightarrow {}^5I_8$ (red). Obviously, the emission is dominated by $^5F_4$, $^5S_2 \rightarrow {}^5I_8$ transitions and gives a green luminescence with CIE chromaticity coordinate ($x = 0.3211$, $y = 0.6518$) (Fig. 8, point e). The proposed UC mechanism in the Yb^{3+}/Ln^{3+} (Ln^{3+} = Er, Tm, Ho) is described in the energy diagram, as shown in Fig. 9D. The excitation signal (980 nm) is initially absorbed by Yb^{3+} ions to raise the $^2F_{7/2}$ to the $^2F_{5/2}$ excited state. For Lu_2O_3:Yb, Er (Fig. 9D), the $^4I_{11/2}$ energy level of the Er^{3+} ions is excited by an initial energy transfer from Yb^{3+} ions in the $^2F_5$ state. Meanwhile, some of the excited Er^{3+} ions relax rapidly to the low-lying levels of the $^4I_{13/2}$ states. Once these states are populated, a subsequent 980 nm photon transferred from the excited-state Yb^{3+} ions can populate a higher $^4F_{7/2}$ energetic state of the Er^{3+} ions. The Er^{3+} ions can then decay nonradiatively to the low-lying $^2H_{11/2}$ and $^4S_{3/2}$ states of the Er^{3+} ions, which result in the dominant green $^2H_{11/2} \rightarrow {}^4I_{15/2}$ and $^4S_{3/2} \rightarrow {}^4I_{15/2}$ emission or further relax and populate a red $^4F_{9/2} \rightarrow {}^4I_{15/2}$ emission. Similarly, in the case of Lu_2O_3:Yb^{3+}/Tm^{3+} and Lu_2O_3:Yb^{3+}/Ho^{3+}, the energy levels of the Tm^{3+} and Ho^{3+} ions are also excited by an initial energy transfer from the excited state Yb^{3+} ions, then a few subsequent energy transfer processes from Yb^{3+} ions populate the upper Tm^{3+} and Ho^{3+} levels, resulting in the various emissions of Tm^{3+} and Ho^{3+}.

The CL properties of the above Lu_2O_3:Ln^{3+} (Ln^{3+} = Eu, and Tb) phosphors were also investigated. Under low-voltage electron beam excitation, the as-prepared Lu_2O_3:Eu^{3+} and Lu_2O_3:Tb^+ samples also exhibit the strong red and green emissions as the UV excitation, respectively. Fig. 10A and D shows the typical CL spectra of Lu_2O_3:Eu^{3+} and Lu_2O_3:Tb^+ phosphors under the excitation of electron beam (accelerating voltage = 3 kV; filament

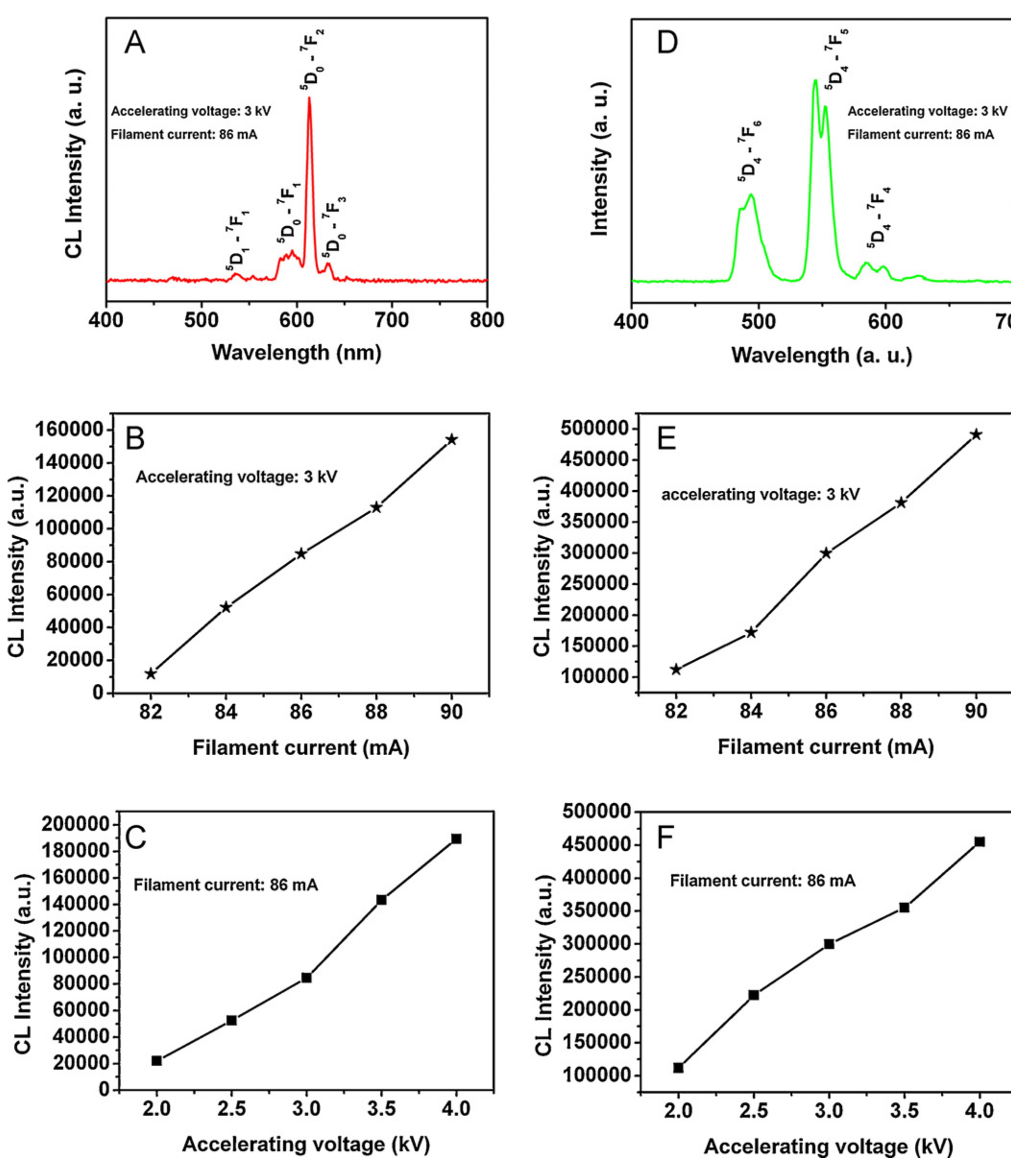

Fig. 10. Typical cathodoluminescence spectra of the Lu_2O_3:Ln^{3+} and the cathodoluminescence intensity of the sample as a function of filament current and accelerating voltage (A–C for Eu^{3+}, and D–F for Tb^{3+}).

current = 86 mA), which have similar shapes as the PL emission spectra. However, the relative intensity of peaks in photoluminescence and cathodoluminescence spectra varies, which may be caused by the different excitation mechanism. The CL emission intensities for the $Lu_2O_3:Eu^{3+}$ and $Lu_2O_3:Tb^{3+}$ samples have been investigated as a function of the accelerating voltage and the filament current, as shown in Fig. 10. Under a 3 kV electron beam excitation, the CL intensity increases with increasing the filament current from 82 to 90 mA. Similarly, when the filament current is fixed at 86 mA, the CL intensity increased with raising the accelerating voltage from 2.0 to 4.0 kV. For cathodoluminescence, the Ln^{3+} ions are excited by the plasma produced by the incident electrons. The electron penetration depth can be estimated by:

$$L\ [\text{Å}] = 250\left(\frac{A}{r}\right)\left(\left(\frac{E}{Z}\right)^{1/2}\right)^{n} \quad (5)$$

where $n = 1.2/(1–0.29\log_{10}Z)$, A is the atomic or molecular weight of the material, ρ is the bulk density, Z is the atomic number or the number of electrons per molecule in the case compounds, and E is the accelerating voltage (kV) [57]. With the increase of accelerating voltage, more plasma will be produced by the incident electrons, resulting in more Eu^{3+}/Tb^{3+} being excited and higher CL intensity. The increase in electron energy is attributed to deeper penetration of electron into the phosphor body which is governed by Eq. (5). The deeper penetration of electrons in the phosphor body results in an increase in electron–solid interaction volume in which excitation of Ln^{3+} ions is responsible for the light emission. Therefore, an increase in interaction volume (which effectively determines the generation of light inside the phosphor) with an increase in electron energy brings about an increase in CL brightness of $Lu_2O_3:Eu^{3+}/Tb^{3+}$ particles [58]. Due to the strong low-voltage CL intensity of $Lu_2O_3:Eu^{3+}/Tb^{3+}$ phosphors, they may find possible applications in field emission display devices.

4. Conclusion

In summary, multicolored and monodisperse $Lu_2O_3:Ln^{3+}$ ($Ln^{3+} = Eu^{3+}$, Tb^{3+}, Yb^{3+}/Er^{3+}, Yb^{3+}/Tm^{3+}, and Yb^{3+}/Ho^{3+}) microspheres with a uniform diameter of 50 nm were successfully synthesized by a urea-assisted homogeneous precipitation method which follows by a subsequent calcination process. The as-prepared $Lu_2O_3:Ln^{3+}$ phosphors show abundant luminescent properties through doping different Ln^{3+} ions under ultraviolet-visible light excitation, low-voltage electron beams excitation, and NIR light excitation, which have potential applications in lighting, displays, or biomedicine.

References

[1] M.J. MacLachlan, I. Manners, G.A. Ozin, Adv. Mater. 12 (2000) 675.
[2] H. Zhou, Y. Mao, S.S. Wong, Chem. Mater. 19 (2007) 5238.
[3] Y.B. Mao, T.J. Park, F. Zhang, H.J. Zhou, S.S. Wong, Small 3 (2007) 1122.
[4] Z.H. Xu, J. Yang, Z.Y. Hou, C.X. Li, C.M. Zhang, S.S. Huang, J. Lin, Mater. Res. Bull. 44 (2009) 1850.
[5] Z.Y. Cheng, R.B. Xing, Z.Y. Hou, S.S. Huang, J. Lin, J. Phys. Chem. C 114 (2010) 9883.
[6] M.S. Palmer, M. Neurock, M.M. Olken, J. Am. Chem. Soc. 124 (2002) 8452.
[7] Z.Y. Hou, P.P. Yang, C.X. Li, L.L. Wang, H.Z. Lian, Z.W. Quan, J. Lin, Chem. Mater. 20 (2008) 6686.
[8] X. Wang, Y.D. Li, Chem. Eur. J. 9 (2003) 5627.
[9] Q. Tang, Z.P. Liu, S. Li, S.Y. Zhang, X.M. Liu, Y.T. Qian, J. Cryst. Growth 259 (2003) 208.
[10] C.X. Li, J. Yang, Z.W. Quan, P.P. Yang, D.Y. Kong, J. Lin, Chem. Mater. 19 (2007) 4933.
[11] C.X. Li, J. Lin, J. Mater. Chem. 20 (2010) 6831.
[12] M. Nichkova, D. Dosev, S.J. Gee, B.D. Hammock, I.M. Kennedy, Anal. Chem. 77 (2005) 6864.
[13] Z.Y. Cheng, P.A. Ma, Z.Y. Hou, W.X. Wang, Y.L. Dai, X.F. Zhai, J. Lin, Dalton Trans. 41 (2012) 1481.
[14] Z.Y. Hou, L.L. Wang, H.Z. Lian, R.T. Chai, C.M. Zhang, Z.Y. Cheng, J. Lin, J. Solid State Chem. 182 (2009) 698.
[15] C.X. Li, Z.W. Quan, J. Yang, P.P. Yang, J. Lin, Inorg. Chem. 46 (2007) 6329.
[16] P.A. Tanner, L.S. Fu, B.M. Cheng, J. Phys. Chem. C 113 (2009) 10773.
[17] Z.Y. Hou, C.X. Li, J. Yang, H.Z. Lian, P.P. Yang, R.T. Chai, Z.Y. Cheng, J. Lin, J. Mater. Chem. 19 (2009) 2737.
[18] Z.Y. Cheng, J. Lin, CrystEngComm 12 (2010) 2646.
[19] Z.Y. Hou, Z.Y. Cheng, G.G. Li, W.X. Wang, C. Peng, C.X. Li, P.A. Ma, D.M. Yang, X.J. Kang, J. Lin, Nanoscale 3 (2011) 1568.
[20] C.X. Li, J. Yang, P.P. Yang, H.Z. Lian, J. Lin, Chem. Mater. 20 (2008) 4317.
[21] H. Wang, C.K. Duan, P.A. Tanner, J. Phys. Chem. C 112 (2008) 16651.
[22] E.M. Goldys, K. Drozdowicz-Tomsia, S. Jinjun, D. Dosev, I.M. Kennedy, S. Yatsunenko, M. Godlewski, J. Am. Chem. Soc. 128 (2006) 14498.
[23] R.J. Kennedy, J.C. Campbell, J. Phys. C: Solid State Phys. 13 (1980) 5341.
[24] J.W. Wang, P.A. Tanner, J. Am. Chem. Soc. 132 (2010) 947.
[25] D.L. Shi, J. Lian, W. Wang, G.K. Liu, P. He, Z.Y. Dong, L.M. Wang, R.C. Ewing, Adv. Mater. 18 (2006) 189.
[26] A.J. Kenyon, Prog. Quantum Electron. 26 (2002) 225.
[27] Y. Hasegawa, S. Thongchant, Y. Wada, H. Tanaka, T. Kawai, T. Sakata, H. Mori, Y. Shozo, Angew. Chem. Int. Ed. 41 (2002) 2073.
[28] H. Tokoro, S. Fujii, T. Oku, J. Mater. Chem. 14 (2004) 253.
[29] O.V. Buyevskaya, D. Wolf, M. Baerns, Catal. Today 62 (2000) 91.
[30] C.C. Huang, C.H. Su, W.M. Li, T.Y. Liu, J.H. Chen, C.S. Yeh, Adv. Funct. Mater. 19 (2009) 249.
[31] P. Yang, S. Gai, Y. Liu, W. Wang, C. Li, J. Lin, Inorg. Chem. 50 (2011) 2182.
[32] J. Lu, K. Takaichi, T. Uematsu, A. Shirakawa, M. Musha, K. Ueda, H. Yagi, T. Yanagitani, A.A. Kaminskii, Appl. Phys. Lett. 81 (2002) 4324.
[33] M. Nyk, D. Hreniak, W. Strezk, J. Misiewicz, E. Zych, Opt. Mater. 26 (2004) 129.
[34] L.Q. An, J. Zhang, M. Liu, S. Chen, S.W. Wang, Opt. Mater. 30 (2008) 957.
[35] S. Polizzi, S. Bucella, A. Speghini, F. Vetrone, R. Naccache, J.C. Boyer, J.A. Capobianco, Chem. Mater. 16 (2004) 1330.
[36] F. Vetrone, J.C. Boyer, J.A. Capobianco, J. Phys. Chem. B 106 (2002) 5622.
[37] L.Q. An, J. Zhang, M. Liu, S.W. Wang, J. Lumin. 122–123 (2007) 125.
[38] Q.W. Chen, Y. Shi, L.Q. An, S.W. Wang, J.Y. Chen, J.L. Shi, J. Eur. Ceram. Soc. 27 (2007) 191.
[39] M. Galceran, M.C. Pujol, M. Aguilo, F. Diaz, Mater. Sci. Eng. B 146 (2008) 7.
[40] J. Guang, Y.H. Zheng, K. Liu, Y.H. Song, H.P. You, H.J. Zhang, J. Phys. Chem. C 113 (2009) 153.
[41] J. Yang, C.M. Zhang, C. Peng, C.X. Li, L.L. Wang, R.T. Chai, J. Lin, Chem. Eur. J. 15 (2009) 4649.
[42] L.S. Wang, Y.H. Zhou, Z.W. Quan, J. Lin, Mater. Lett. 59 (2005) 1130.
[43] E. Matijević, W.P. Hsu, J. Colloid Interface Sci. 118 (1987) 506.
[44] S. Lechevallier, P. Lecante, R. Mauricot, H. Dexpert, J. Dexpert-Ghys, H.K. Kong, G.L. Law, K.L. Wong, Chem. Mater. 22 (2010) 6153.
[45] I.F. Li, C.H. Su, H.S. Sheu, H.C. Chiu, Y.W. Lo, W.T. Lin, J.H. Chen, C.S. Yeh, Adv. Funct. Mater. 18 (2008) 766.
[46] J. Yang, C.X. Li, Z.W. Quan, C.M. Zhang, P.P. Yang, Y.Y. Li, C.C. Yu, J. Lin, J. Phys. Chem. C 112 (2008) 12777.
[47] L.Q. An, J. Zhang, M. Liu, S.W. Wang, J. Lumin. 125 (2007) 122.
[48] Z.G. Yan, C.H. Yan, J. Mater. Chem. 18 (2008) 5046.
[49] L.X. Yu, H.W. Song, Z.X. Liu, L.M. Yang, S.Z. Lu, Phys. Chem. Chem. Phys. 8 (2006) 303.
[50] J.X. Wan, Z.H. Wang, X.Y. Chen, L. Mu, Y.T. Qian, J. Cryst. Growth 284 (2005) 538.
[51] X.C. Wu, Y.R. Tao, F. Gao, L. Dong, Z. Hu, J. Cryst. Growth. 277 (2005) 643.
[52] J. Yang, Z.W. Quan, D.Y. Kong, X.M. Liu, J. Lin, Cryst. Growth Des. 7 (2007) 730.
[53] J. Yang, C.X. Li, Z.W. Quan, C.M. Zhang, P.P. Yang, Y.Y. Li, C.C. Yu, J. Lin, J. Phys. Chem. C 1112 (2008) 12777.
[54] G. Yi, B. Sun, F. Yang, D. Chen, Y. Zhou, J. Cheng, Chem. Mater. 14 (2002) 2910.
[55] K.W. Kramer, D. Biner, G. Frei, H.U. Gudel, M.P. Hehlen, S.R. Luthi, Chem. Mater. 16 (2004) 1244.
[56] Z. Chen, W. Bu, N. Zhang, J. Shi, J. Phys. Chem. C 112 (2008) 4378.
[57] C. Feldman, Phys. Rev. 117 (1960) 455.
[58] D. Kumar, K.G. Cho, Z. Chen, V. Craciun, P.H. Holloway, R.K. Singh, Phys. Rev. B. 60 (1999) 13331.